SUPPORTING INFORMATION

An Organic-Inorganic Heterojunction Electrocatalyst for Highly Efficient Urea Oxidation

Tzu-Ho Wu,[a] Zi-Ting Qiu,[a] Chih-Ning Hsieh,[a] Zi-Ting Chen,[b] Tzu-Wei Wang,[c]*

*Po-Liang Liu,[c,d] and Rong-Ho Lee[b,e]**

[a] Department of Chemical and Materials Engineering, National Yunlin University of Science and Technology, Yunlin 64002, Taiwan. E-mail: wutzu@yuntech.edu.tw

[b] Department of Chemical Engineering, National Chung Hsing University, Taichung 40227, Taiwan. E-mail: rhl@dragon.nchu.edu.tw

[c] Graduate Institute of Precision Engineering, National Chung Hsing University, Taichung 40227, Taiwan

[d] Department of Applied Materials and Optoelectronic Engineering, National Chi Nan University, Nantou 54561, Taiwan

[e] Department of Chemical Engineering and Materials Science, Yuan Ze University, Taoyuan 320315, Taiwan

1. Experimental Procedures

Chemicals.

4-Aminobenzonitrile, p-bromobenzonitrile, trifluoromethanesulfonic acid, n-BuLi (2.5 M in hexane), N-formylpiperidine, 1,4-dioxane, mesitylene, acetic acid (HOAc), nickel(II) nitrate, urea, ethanol, and other chemicals were purchased from Sigma-Aldrich, Acros, Alfa, and TCI Chemical and used as received. 2,4,6-tris(4-aminophenyl)triazine (TPT-3NH_2) and 2,4,6-tris(4-formylphenyl)-1,3,5-triazine (TPT-3CHO) were prepared according to the reported procedures.[1] Multi-walled carbon nanotubes (CNT) were purchased from Uni-onward, Taiwan, and the powders were functionalized by acid treatment prior to use.[2]

Synthesis of COF and COF/CNT.

According to our previous work, the triazine-based covalent organic framework sample was prepared through Schiff base condensations.[3] Briefly, TPT-3NH_2 (53.1 mg) and TPT-3CHO (59.0 mg) were mixed in 1,4-dioxane/mesitylene/6 M HOAc (v/v/v = 1/1/0.24) in a Pyrex tube. It was degassed by applying three freeze/pump/thaw cycles and then heated at 120 ^oC for 3 days. The resulting precipitate was collected by suction filtration and washed several times with tetrahydrofuran (THF), acetone, and methanol. The TPTP-COF sample (denoted as COF) was obtained after drying at 120 ^oC under vacuum for 24 h. The COF/CNT sample was prepared followed by the same procedures but with the addition of CNT (30 wt.%) in the precursor solution. For comparison, 15 wt.% CNT was also used to prepare the COF/15%-CNT sample.

Synthesis of $Ni(OH)_2$, $Ni(OH)_2$/COF, $Ni(OH)_2$/CNT, and $Ni(OH)_2$/COF/CNT

$Ni(OH)_2$ was prepared by chemical precipitation method. Nickel(II) nitrate (0.45 g) and urea (3 g) were mixed in deionized water in a conical flask, and the solution was maintained at 80 ^oC for 2 h. Afterward, the resulting precipitate was washed with deionized water and ethanol. The $Ni(OH)_2$ powder sample was collected after drying at 60 ^oC overnight. It followed the same procedures to prepare $Ni(OH)_2$/COF, $Ni(OH)_2$/CNT, $Ni(OH)_2$/COF/CNT, and $Ni(OH)_2$/COF/15%-CNT nanocomposites but with the addition of the as-prepared COF, CNT, COF/CNT, and COF/15%-CNT (50 mg) into the nickel nitrate/urea mixture, respectively.

Materials characterization.

X–ray diffraction (XRD, Rigaku MiniFlex600), Raman microscopy (Renishaw, InVia confocal microscope with 633 nm laser source), X-ray photoelectron spectroscopy (XPS, ULVAC-PHI 5000 VersaProbe III with ultraviolet photoelectron spectroscopy,

UPS), scanning electron microscope (SEM, JEOL JSM-7610F Plus equipped with energy-dispersive X-ray spectroscopy (EDS)), transmission electron microscope (TEM, JEOL JEM-2010), thermogravimetric analysis (TGA, PerkinElmer TGA-4000 tested under airflow of 20 ml min^{-1} at a ramping rate of 10 ^{o}C min^{-1}), ultraviolet–visible (UV-vis) spectroscopy (Perkin Elmer Lambda 850), and Hall-effect Analyzer (Agilent, HP 4145B with the current resolution ≤100 fA) were used to analyze the synthesized samples.

Electrochemical measurements.

The electrochemical tests were carried out by a three-electrode configuration on CH Instruments 6273D. was prepared by dropping the slurry onto Ni foam (NF) substrate with the slurry made of the prepared sample ($Ni(OH)_2$, COF/CNT, $Ni(OH)_2$/COF, $Ni(OH)_2$/CNT, $Ni(OH)_2$/COF/CNT, or $Ni(OH)_2$/COF/15%-CNT), Super P carbon, and poly(vinylidene difluoride) binder in a weight ratio of 8:1:1. The mass loading of the electrode is controlled to ~1.25 mg cm^{-2} (~1.0 mg cm^{-2} for the active component). Hg/HgO and Pt wire were as reference and counter electrodes, respectively. 1 M KOH with 0.33 M urea was used as the electrolyte for the urea oxidation reaction (UOR), while 1 M KOH served as the electrolyte for the oxygen evolution reaction (OER). All the reported potential values were converted with respect to a reversible hydrogen electrode (RHE) according to the equation ($E_{RHE} = E_{Hg/HgO} + 0.098 + 0.059$ pH). Linear sweep voltammetry (LSV) was conducted at 5 mV s^{-1}, and 80% *iR* compensation was applied to the LSV measurements and the corresponding Tafel analysis. Cyclic voltammetry (CV) was performed between 0.82 and 1.02 V from 10 to 100 mV s^{-1} to evaluate double-layer capacitance (C_{DL}). Chronoamperometry (CA) was undertaken at 1.40 V for 500 s for evaluating the reaction rate constant, while the Coulombic efficiencies were estimated from the current responses in UOR and OER by holding at the potentials between 1.27 and 1.47 V (interval of 20 mV, lasting 500 s for each step). Chronopotentiometry (CP) was evaluated at 20 mA cm^{-2} for 24 h and 50 mA cm^{-2} for 8 h.

***In situ* electrochemical Raman measurements.**

In situ Raman study was carried out in a commercial Raman cell (purchased from Shanghai Chuxi Industry Co., Ltd) using Hg/HgO as the reference electrode and a Pt wire as the counter electrode. 1 M KOH with 0.33 M urea was used as the electrolyte. Again, the Raman spectra were collected with a Raman microscope (Renishaw, InVia) using a 633 nm laser source. For potential dependent *in situ* experiments, the Raman spectra were collected at different potentials starting from open-circuit potential (OCP) to 1.48 V (vs. RHE). For each spectrum, the $Ni(OH)_2$/COF/CNT electrode was pre-

polarized for 100 s and held during the spectral acquisition (~250 s) with the ranges of 400-600 and 950-1050 cm^{-1}. For time dependent *in situ* experiments, the $Ni(OH)_2$/COF/CNT electrode was pre-polarized at 1.52 V (vs. RHE) for 1000 s. Then, the Raman spectra were recorded at rest conditions (i.e., without applied potential). To obtain better time resolved spectra, the detection range was adjusted to 400-600 cm^{-1} corresponding to the acquisition time of ~60 s for each spectrum.

Theoretical calculations.

This study employed first-principles calculations based on density functional theory (DFT) to optimize geometry on $Ni(OH)_2$ and COF structures. The theoretical techniques used included the generalized gradient approximation (GGA) and the Perdew-Wang (PW91) correction.[4-7] Simulations were conducted using the Vienna *Ab Initio* Simulation Package (VASP) to find equilibrium crystal structures (refer to **Figure S20** and **Table S2**). The $Ni(OH)_2$ unit cell model comprises five atoms: one Ni atom, two O atoms, and two H atoms, with a space group of $P\bar{3}m1$. The calculations were set with a plane wave cut-off energy of 450 eV and *k*-points configured as a 7 × 7 × 6 Gamma-centered grid. The valence electron configurations were Ni $3d^8$ $4s^2$, O $2s^2$ $2p^4$, and H $1s^1$. The COF unit cell model consists of 81 atoms: nine N atoms, 45 C atoms, and 27 H atoms, with a space group of *P*6/*m*. Similarly, the calculations were set with a plane wave cut-off energy of 450 eV and *k*-points configured as a 1 × 1 × 7 Gamma-centered grid. The valence electron configurations were N $2s^2$ $2p^3$, C $2s^2$ $2p^2$, and H $1s^1$. For the self-consistent electronic calculations for electronic properties (**Figure S21**), the $Ni(OH)_2$ model used *k*-points of 7 × 7 × 6 and a cut-off energy of 450 eV, with total energy convergence set to 1×10^{-5} eV/atom. The path in the first Brillouin zone for the wave number was set sequentially as G (0, 0, 0) → A (0, 0, 0.5) → H (0.333, 0.333, 0.5) → K (0.333, 0.333, 0) → G (0, 0, 0) → M (0.5, 0, 0) → L (0.5, 0, 0.5) → H (0.333, 0.333, 0.5). For COF, the *k*-points were set as 1 × 1 × 7, with a cut-off energy of 450 eV and total energy convergence set to 1×10^{-5} eV/atom. The path in the first Brillouin zone was set as G (0, 0, 0) → K (0.333, 0.333, 0) → M (0.5, 0, 0) → H (0.333, 0.333, 0.5) → A (0, 0, 0.5) → L (0.5, 0, 0.5) → M (0.5, 0, 0) → G (0, 0, 0). These settings and calculations ensure the precision of the geometry optimization and electronic band structure calculations for the $Ni(OH)_2$ and COF models, providing a reliable theoretical foundation for further understanding the electron transfer behavior between them.

2. Supplementary figures

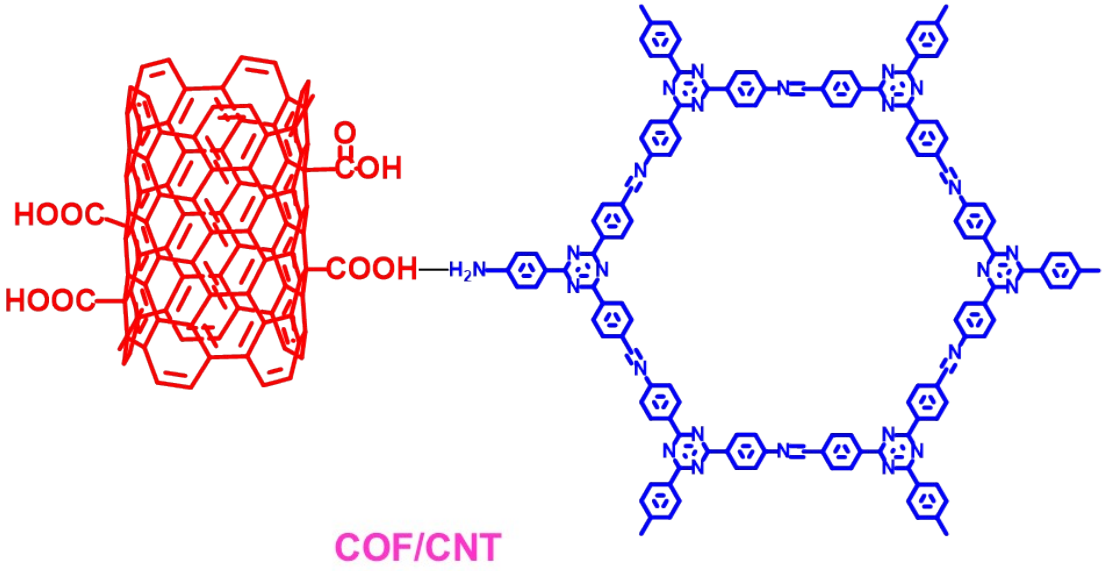

Figure S1. Illustration of the triazine-based COF and CNT nanocomposites (COF/CNT).

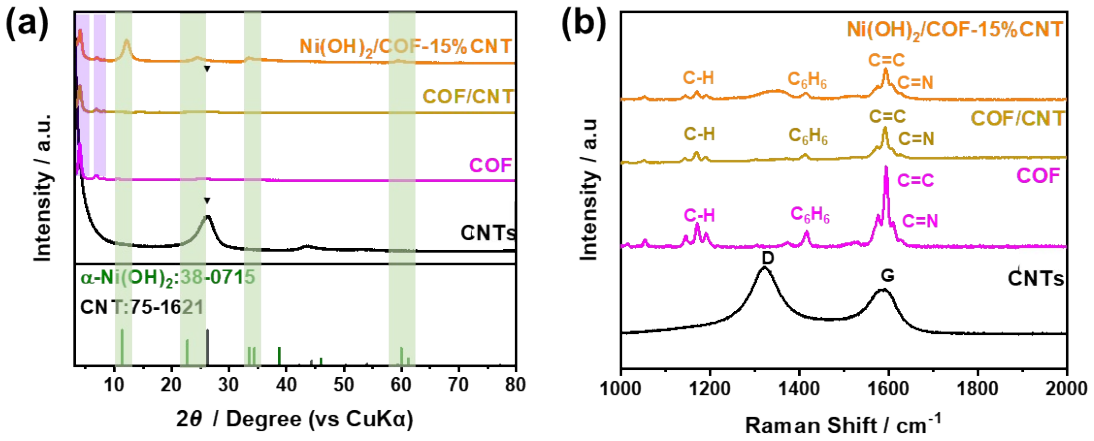

Figure S2. (a) XRD patterns and (b) Raman spectra of CNTs, COF, COF/CNT, and $Ni(OH)_2$/COF-15%CNT.

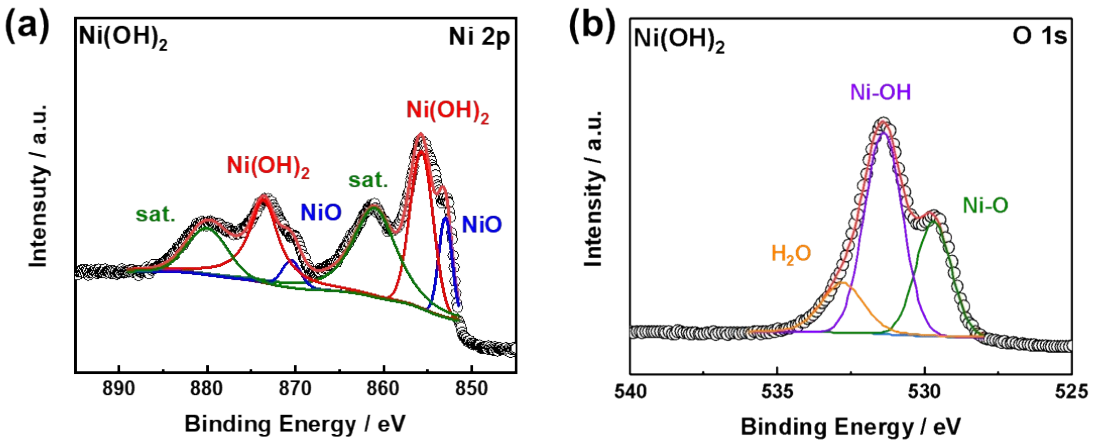

Figure S3. High-resolution XPS (a) Ni 2p and (b) O 1s spectra of $Ni(OH)_2$.

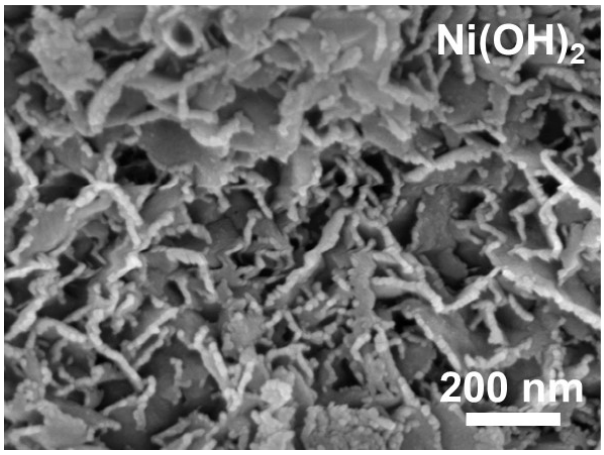

Figure S4. SEM image of $Ni(OH)_2$.

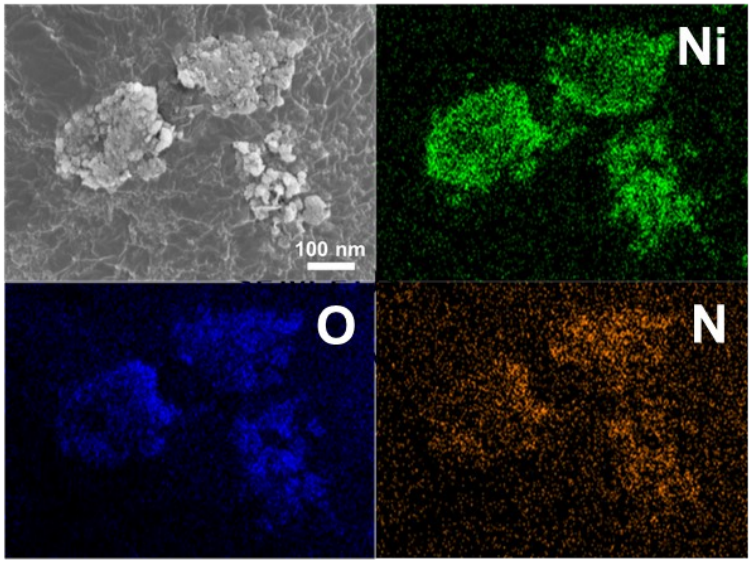

Figure S5. EDS elemental mapping images of $Ni(OH)_2$/COF/CNT.

Thermogravimetric analysis (TGA) was carried out to estimate the $Ni(OH)_2$ contents in the prepared samples. **Figure S6** shows the temperature dependent weight loss profiles for the samples. Both CNT and COF samples can be entirely decomposed by heating to a high temperature at ca. 700 ^oC under an air environment (**Figure S6a-b**). For $Ni(OH)_2$, the weight loss below 100 ^oC can be assigned to the physisorbed water originating from ambient environment, while the weight loss in the region between 100 and 300 ^oC is attributed to the removal of crystal water (**Figure S6c**). The significant weight loss from 300 to ca. 500 ^oC corresponds to dehydration of $Ni(OH)_2$ (i.e., converting $Ni(OH)_2$ into NiO).[8] In this regard, the stoichiometric formula of the pure $Ni(OH)_2$ sample is characterized as $Ni(OH)_2 \cdot 0.25H_2O$. Since the growth of $Ni(OH)_2$ followed the same procedures, it is assumed that the existing $Ni(OH)_2$ component in the $Ni(OH)_2$-based composite samples shares the same stoichiometric formula. The $Ni(OH)_2$-based composite samples show additional weight loss of carbon-based material (COF and/or CNT) in the profiles (**Figure S6d-f**). By excluding the contribution(s) from COF and/or CNT, the $Ni(OH)_2$ contents can also be obtained. Accordingly, the $Ni(OH)_2$ contents are estimated as 32.8, 57.6, and 42.2% in $Ni(OH)_2$/CNT, $Ni(OH)_2$/COF, and $Ni(OH)_2$/COF/CNT, respectively.

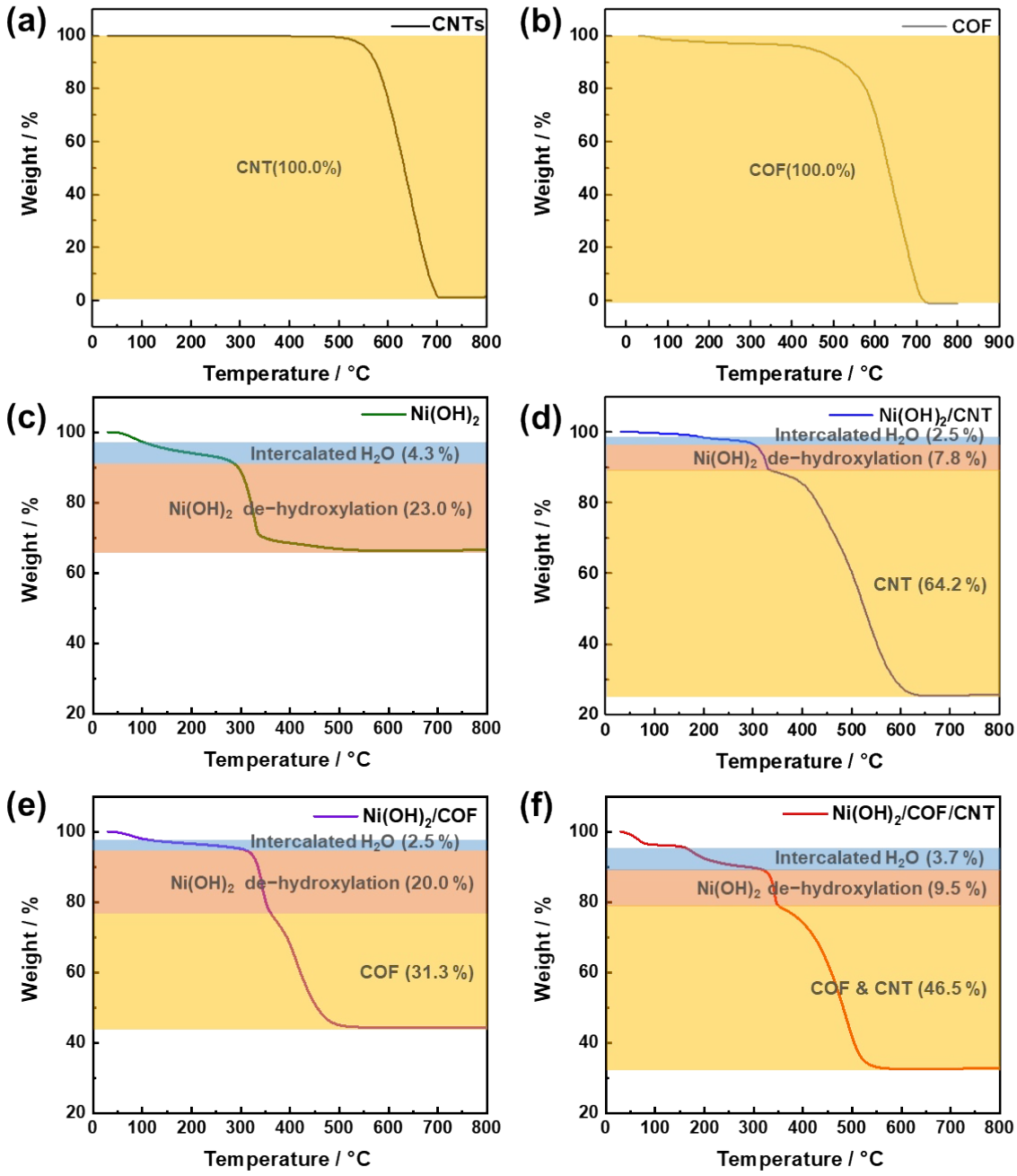

Figure S6. TGA weight loss curves of (a) CNTs, (b) COF, (c) $Ni(OH)_2$, (d) $Ni(OH)_2$/CNT, (e) $Ni(OH)_2$/COF, and (f) $Ni(OH)_2$/COF/CNT.

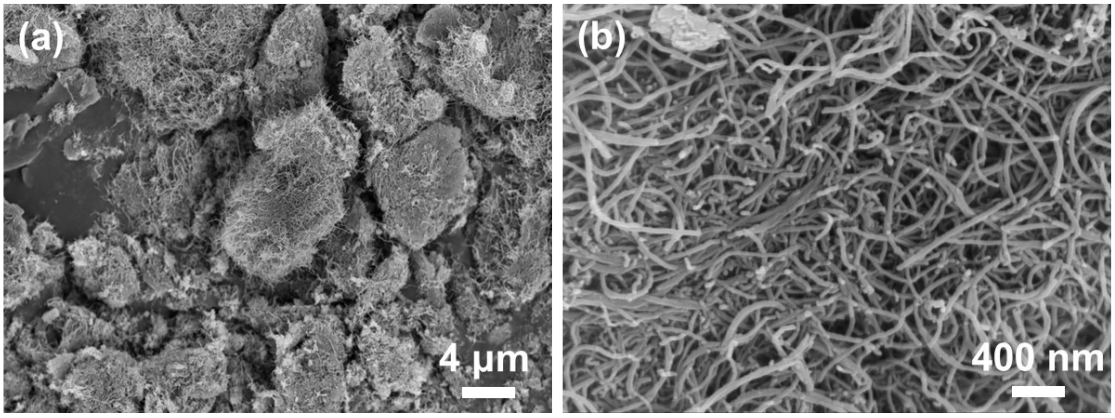

Figure S7. SEM images of $Ni(OH)_2$/CNT.

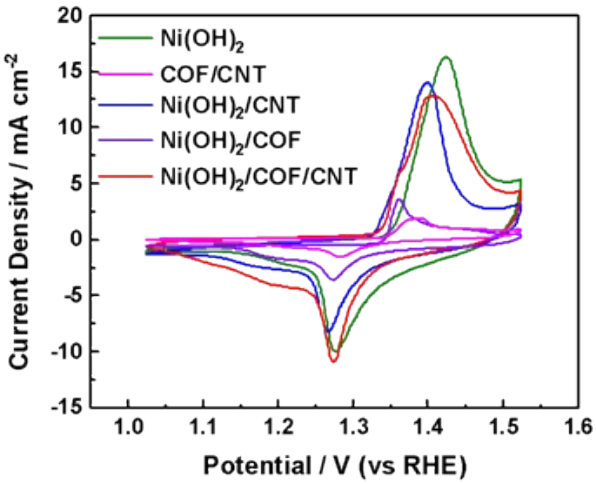

Figure S8. CV curves of $Ni(OH)_2$, COF/CNT, $Ni(OH)_2$/CNT, $Ni(OH)_2$/COF, and $Ni(OH)_2$/COF/CNT in 1 M KOH.

To investigate the effect of the CNT content on electrochemical behavior, two organic-inorganic samples were prepared using different CNT content in the COF/CNT nanocomposites. $Ni(OH)_2$/COF/CNT and $Ni(OH)_2$/COF-15%CNT were prepared from 30 and 15 wt.% CNT in the COF/CNT nanocomposites, respectively. The $Ni(OH)_2$/COF-15%CNT hybrid material is also confirmed to be successfully prepared based on the characterization data (**Figure S2**). By adding more CNT in the composite samples, progressively higher current responses can be observed in the CV (KOH) and LSV (KOH with urea) tests. For the CV tests (**Figure S8** and **Figure S9a**), the anodic peak current density shows the ascending order: $Ni(OH)_2$/COF (3.6 mA cm^{-2}) < $Ni(OH)_2$/COF/CNT-15%CNT (4.9 mA cm^{-2}) < $Ni(OH)_2$/COF/CNT (12.8 mA cm^{-2}). For the LSV tests (**Figure 3a** and **Figure S9b**), the current density at 1.5 V also increases in the following order: (15 mA cm^{-2}) < $Ni(OH)_2$/COF/CNT-15%CNT (38 mA cm^{-2}) < $Ni(OH)_2$/COF/CNT (153 mA cm^{-2}). Similarly, by estimating the $Ni(OH)_2$ content in $Ni(OH)_2$/COF-15%CNT (**Figure S9c**, followed the same procedures as mentioned previously, please refer to page S6), the mass activity of $Ni(OH)_2$ also shows the same trend (**Figure 3c** and **Figure S9d**): $Ni(OH)_2$/COF (26 A $g_{Ni(OH)2}^{-1}$) < $Ni(OH)_2$/COF/CNT-15%CNT (65 A $g_{Ni(OH)2}^{-1}$) < $Ni(OH)_2$/COF/CNT (363 A $g_{Ni(OH)2}^{-1}$). Thus, the above results address that adding sufficient amount of CNT in the composite samples can guarantee satisfactory electron transport in the composite sample for improved electrochemical behavior.

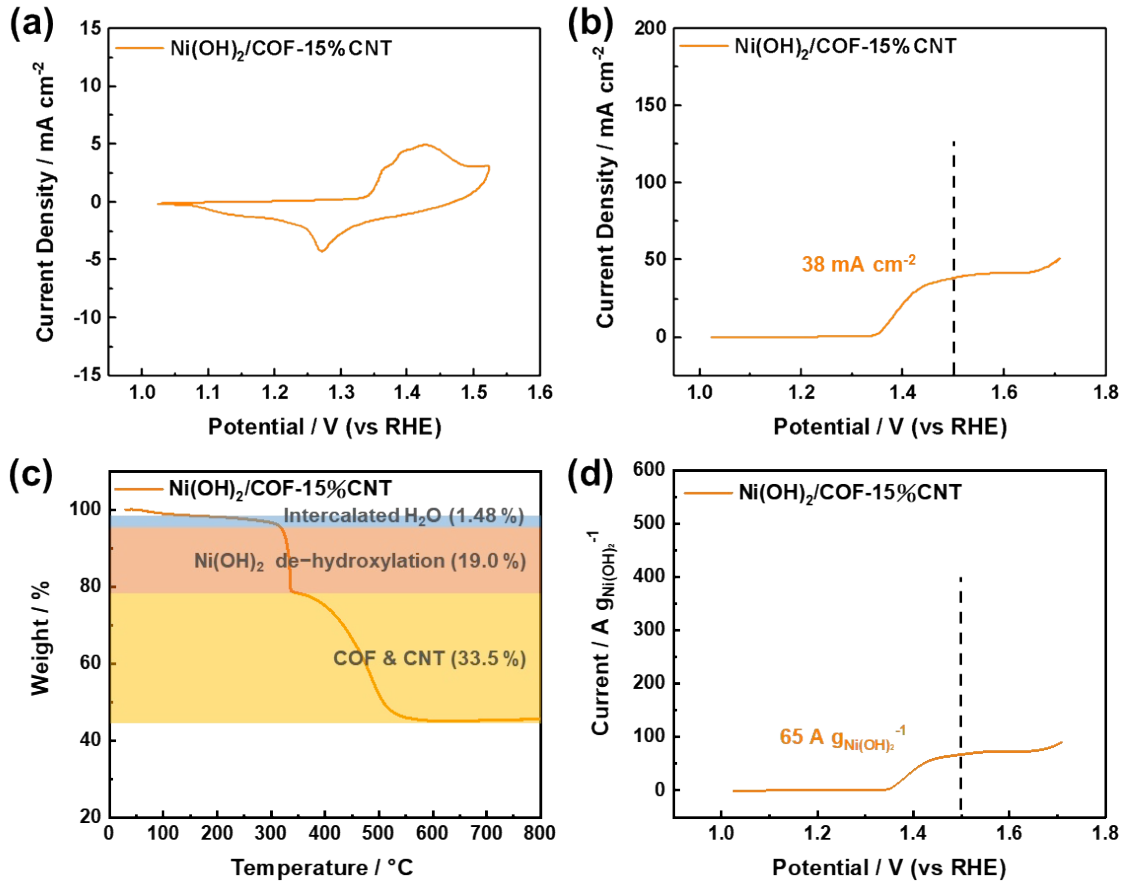

Figure S9. The electrochemical evaluations of $Ni(OH)_2$/COF-15%CNT. (a) CV curve measured in 1 M KOH, (b) *iR*-corrected LSV curve measured in 1 M KOH with 0.33 M urea, (c) TGA weight loss curve, and (d) *iR*-corrected LSV curves with the current responses normalized to the mass of $Ni(OH)_2$.

The turnover frequency (TOF) values were estimated by the following equation:[9]

$$TOF = IN_A/nF\Gamma \quad \text{(S1)}$$

where I, N_A, n, F, Γ represent the current density (A cm^{-2}), the Avogadro number (6.02 $\times 10^{23}$ mol^{-1}), the number of involved electrons (n = 6), the Faraday constant (96485 C mol^{-1}), the number of active sites (cm^{-2}), respectively. The only unknown parameter in this equation is the number of active sites, which can be calculated from the integrated area in the negative sweep of the CV curve in 1 M KOH electrolyte (**Figure S8**). Given the Γ value, the TOF value can be then determined by taking the current density at a certain potential from the LSV curve measured in 1 M KOH with 0.33 M urea (**Figure 3a**). Notably, the reported TOF values for the samples range from 1.4 to 1.6 V in this work (**Figure 3d**). The reason is that UOR and OER are competitive reactions at high anodic potentials. The onset potential toward UOR is 1.37 V for both $Ni(OH)_2$ and $Ni(OH)_2$/COF/CNT, while the onset potentials toward OER are 1.57 and 1.61 V for $Ni(OH)_2$ and $Ni(OH)_2$/COF/CNT, respectively. Thus, the potential window ranging from 1.4 to 1.6 V can better reflect the TOF value corresponding to urea oxidation for the $Ni(OH)_2$/COF/CNT electrocatalyst.

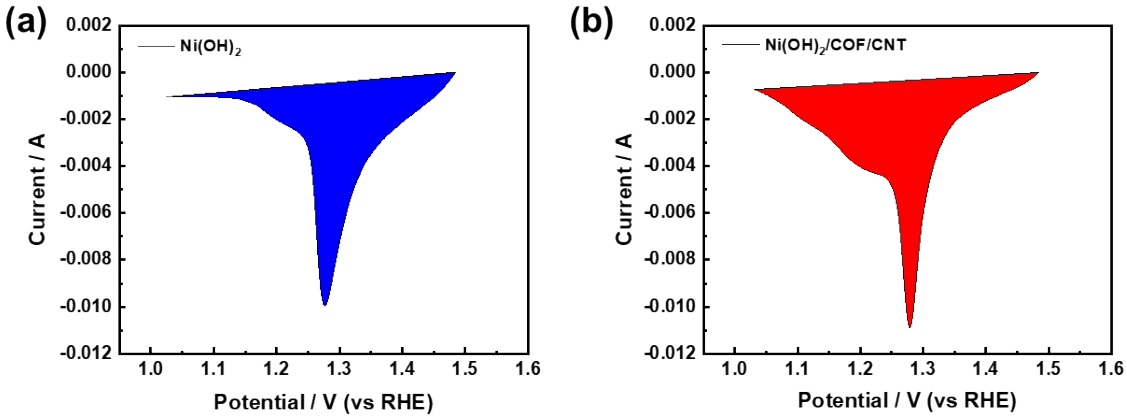

Figure S10. Evaluations of active sites of (a) $Ni(OH)_2$ and (b) $Ni(OH)_2$/COF/CNT in 1 M KOH. Data taken from **Figure S8**.

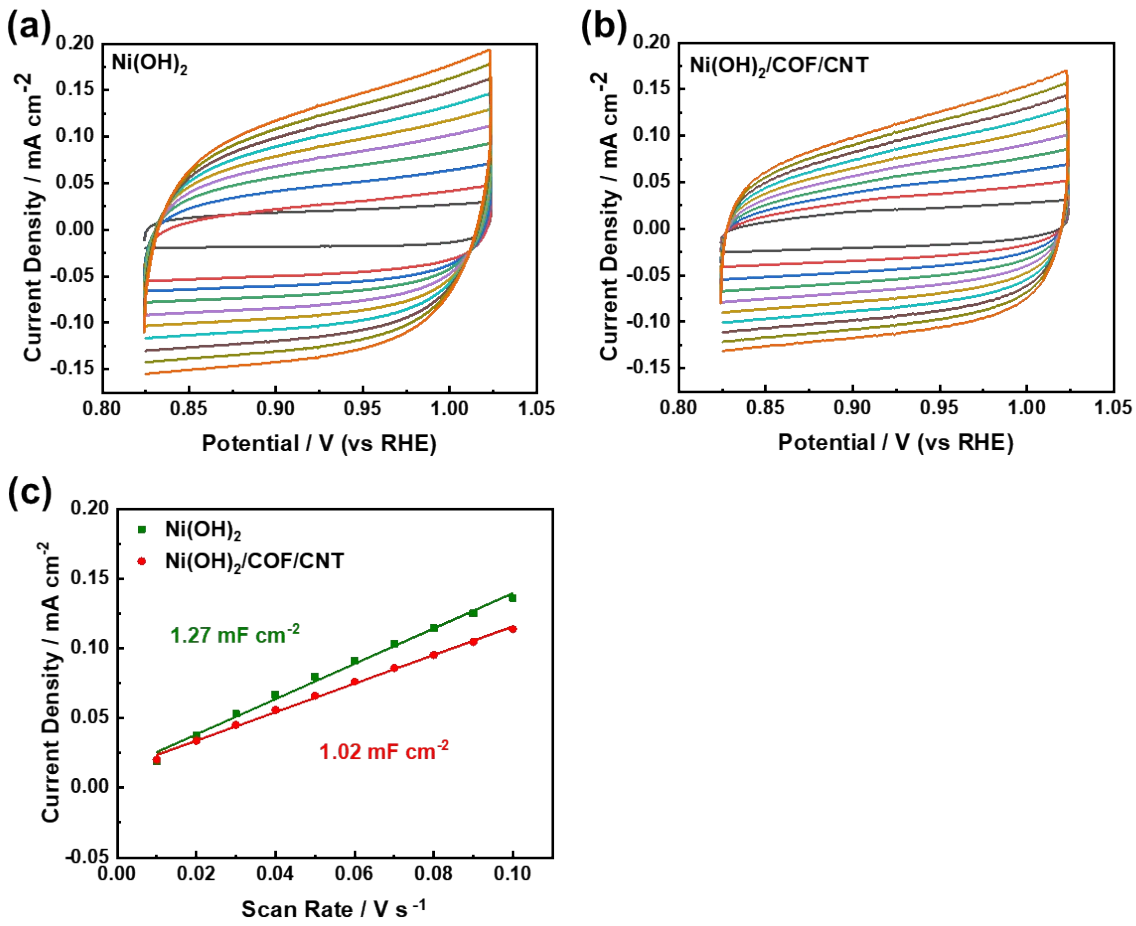

Figure S11. CV curves of (a) $Ni(OH)_2$ and (b) $Ni(OH)_2$/COF/CNT in 1 M KOH with 0.33 M urea. (c) double-layer capacitance evaluations of $Ni(OH)_2$ and $Ni(OH)_2$/COF/CNT.

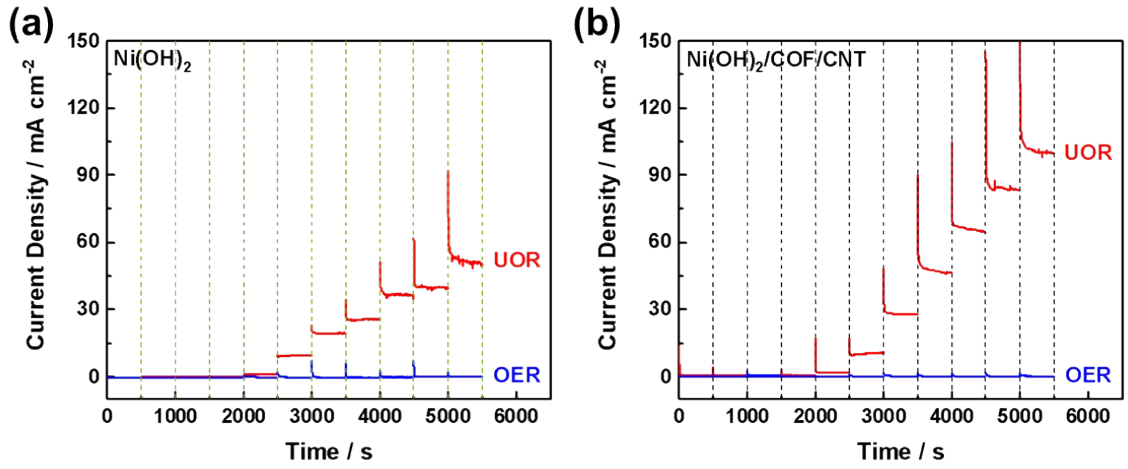

Figure S12. CA curves of (a) $Ni(OH)_2$ and (b) $Ni(OH)_2$/COF/CNT measured between 1.27 and 1.47 V (interval of 20 mV, lasting 500 s for each step) for UOR/OER comparisons.

The reaction rate constant toward UOR (k) can be calculated based on the equation:[10]

$$I_{CAT} / I_L = (\pi k C)^{0.5} t^{0.5} \quad \text{(S2)}$$

where I_{CAT} and I_L are the limiting current densities (mA cm^{-2}) measured in the electrolyte with and without urea, respectively; C is the electrolyte concentration of urea (3.3×10^{-4} mol cm^{-3}); and t is the polarization time (s).

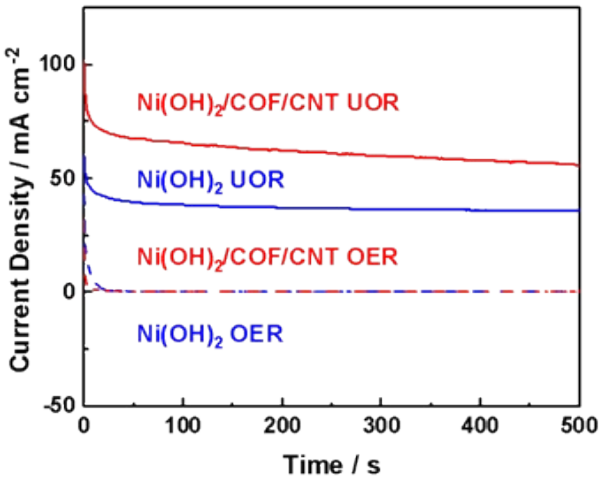

Figure S13. CA curves of $Ni(OH)_2$ and $Ni(OH)_2$/COF/CNT in 1 M KOH with/without 0.33 M urea.

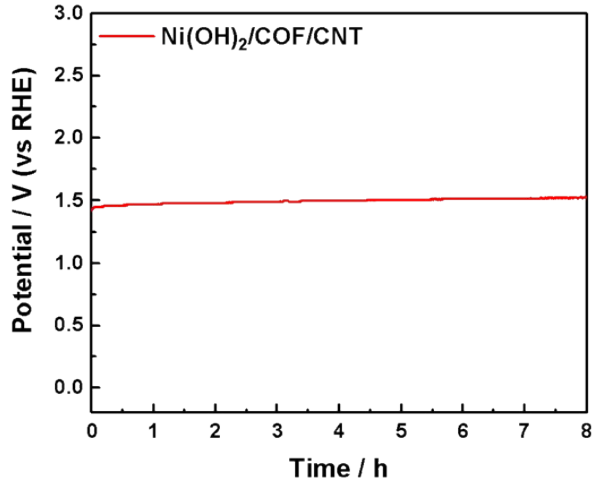

Figure S14. Stability test of $Ni(OH)_2$/COF/CNT at 50 mA cm^{-2} for 8 h in 1 M KOH with/without 0.33 M urea.

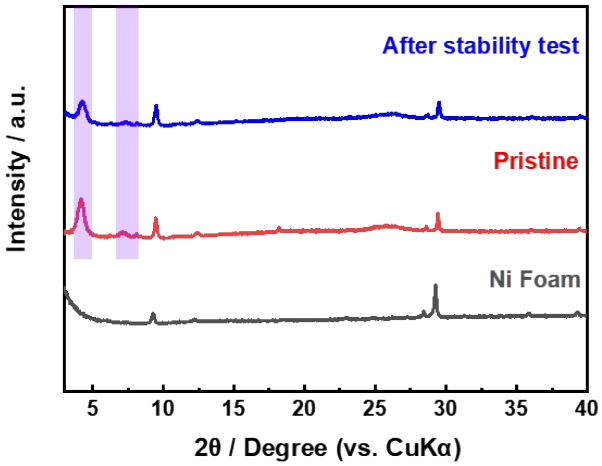

Figure S15. XRD patterns of the Ni foam substrate, pristine $Ni(OH)_2$/COF/CNT, and $Ni(OH)_2$/COF/CNT after the stability test.

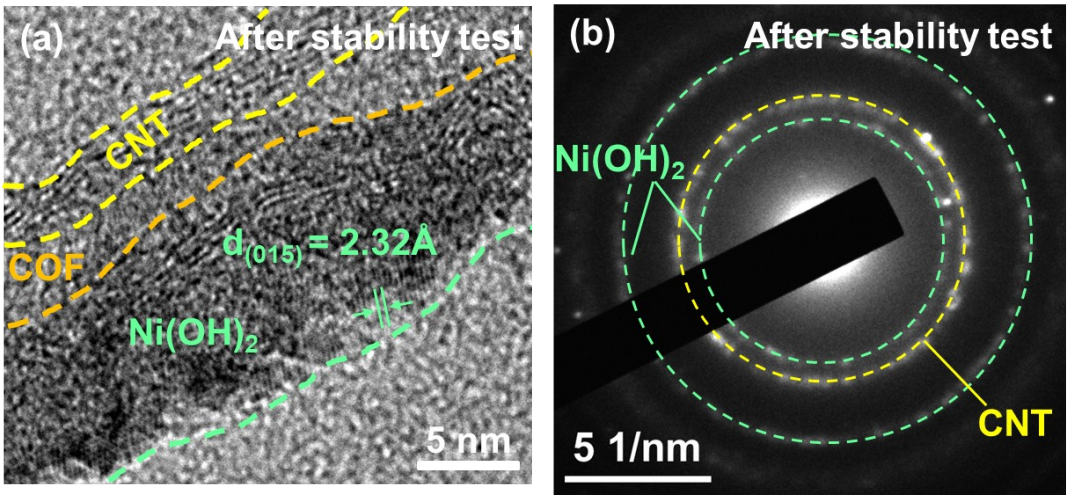

Figure S16. (a) High-resolution TEM images and (b) SAED pattern of $Ni(OH)_2$/COF/CNT after the stability test.

Notably, the strong K signals in **Figure S17c** are from the residual KOH electrolyte salt after the stability test.

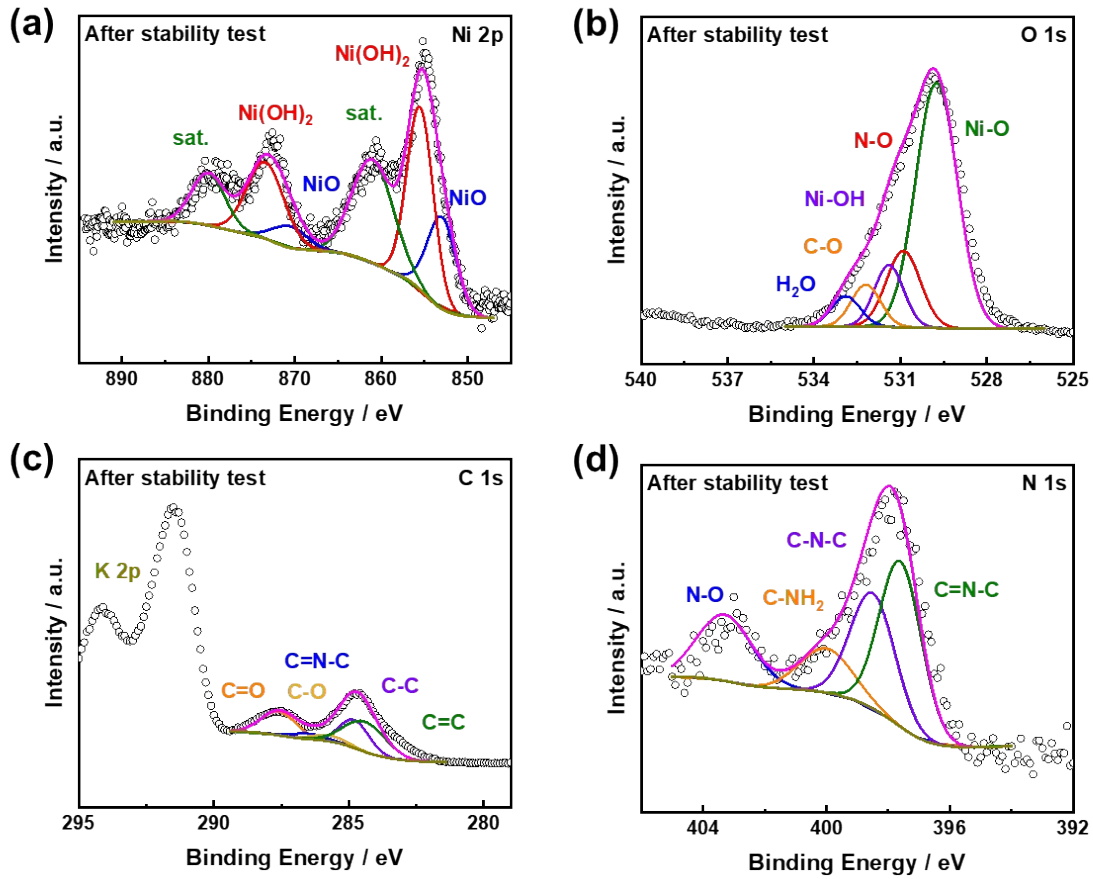

Figure S17. High-resolution XPS (a) Ni 2p, (b) O 1s, (c) C 1s, and (d) N 1s spectra of $Ni(OH)_2$/COF/CNT after the stability test.

Figure S18 shows the UPS spectra of $Ni(OH)_2$ and COF. The secondary electron cut-off (E_{cutoff}) and the onset vaule of the valence band (E_{onset}) can be determined by the higher and lower binding energy regions, respectively. The ionization potential (IP) represents the energy difference between vacuum energy level (E_{vac}) and valence band maximum (E_V). Given the photon energy of the UV source (21.2 eV for He lamp), the IP values can be calculated based on the equation:[11]

$$IP = 21.2 - E_{cutoff} + E_{onset} \quad (S3)$$

Accordingly, the IP values are 4.80 and 5.45 eV for $Ni(OH)_2$ and COF, respectively.

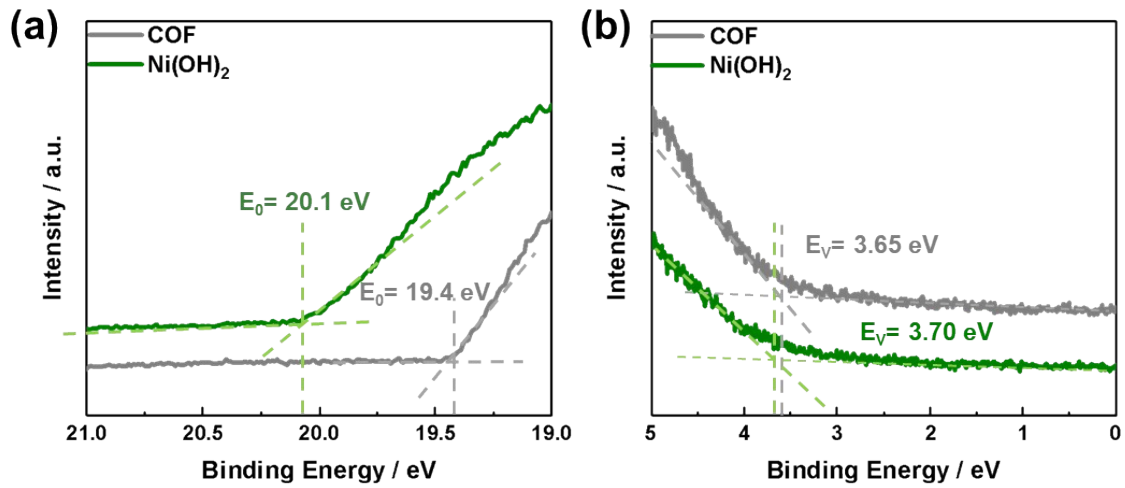

Figure S18. UPS spectra of $Ni(OH)_2$ and COF at (a) higher and (b) binding energy regions.

The characteristic signals of the d-d transition of Ni can be observed in the UV spectrum of $Ni(OH)_2$ (**Figure S19a**). The results align with the previously reported data.[12, 13] For triazine-based COF, the π→π* transition of the conjugated ring systems can be noticed in the UV spectrum of COF (**Figure S19b**). The spectral features agree with the findings in the literature.[14] Followed the reported protocols,[15, 16] the E_g values of $Ni(OH)_2$ and COF can be determined by converting the UV-vis spectra into Tauc's plots. Accordingly, the E_g values are 3.95 and 1.70 eV for $Ni(OH)_2$ and COF, respectively (**Figure S19c,d**).

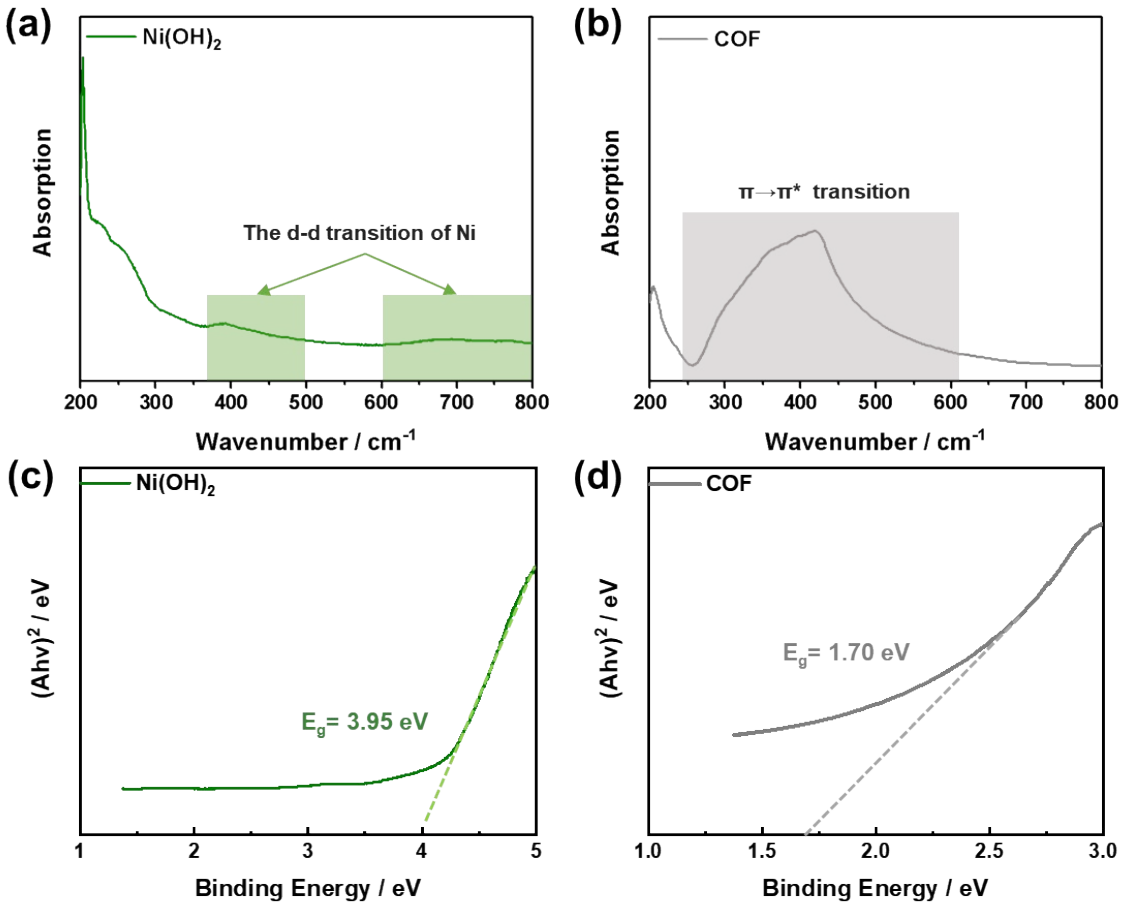

Figure S19. (a,b) UV spectra and (c,d) the corresponding Tauc's plots of (a,c) $Ni(OH)_2$ and (b,d) COF.

To gain deeper insights into the electron transfer behavior between $Ni(OH)_2$ and COF, we constructed models of both materials and performed detailed atomic structure optimizations (**Figure S20** and **Table S2**). Based on the simulation resutls, the electronic properties of the $Ni(OH)_2$ and COF models can be obtained (**Figure S21**). The calculations revealed that the Fermi levels of $Ni(OH)_2$ and COF are 2.5 eV and -0.7 eV, respectively. Upon contact, electrons transfer from the higher Fermi level of $Ni(OH)_2$ to the lower Fermi level of COF until equilibrium is reached. This rearrangement results in lowering the Fermi level of $Ni(OH)_2$ and raising the Fermi level of COF, ultimately achieving a common equilibrium Fermi level. The migration of electrons from $Ni(OH)_2$ to COF creates a positively charged region in $Ni(OH)_2$ and a negatively charged region in COF. This charge distribution establishes an internal electric field allowing rapid electron transfer within the catalyst, which is a characteristic of the *p-n* heterojunction effect.

Notably, in the calculations for three-dimensional $N(OH)_2$ crystals, we use the GGA to handle exchange-correlation energy. This approximation method tends to underestimate the conduction band levels, resulting in a calculated band gap that is lower than the actual value of $Ni(OH)_2$. We also employ the GGA exchange-correlation energy approximation for two-dimensional COF materials to calculate the band gap using the same method. However, due to the quantum confinement effect, the atomic layer thickness of two-dimensional COF materials is skinny, and the movement of electrons and holes is confined to the two-dimensional plane. This confinement leads to an increase in the band gap of two-dimensional COF materials.

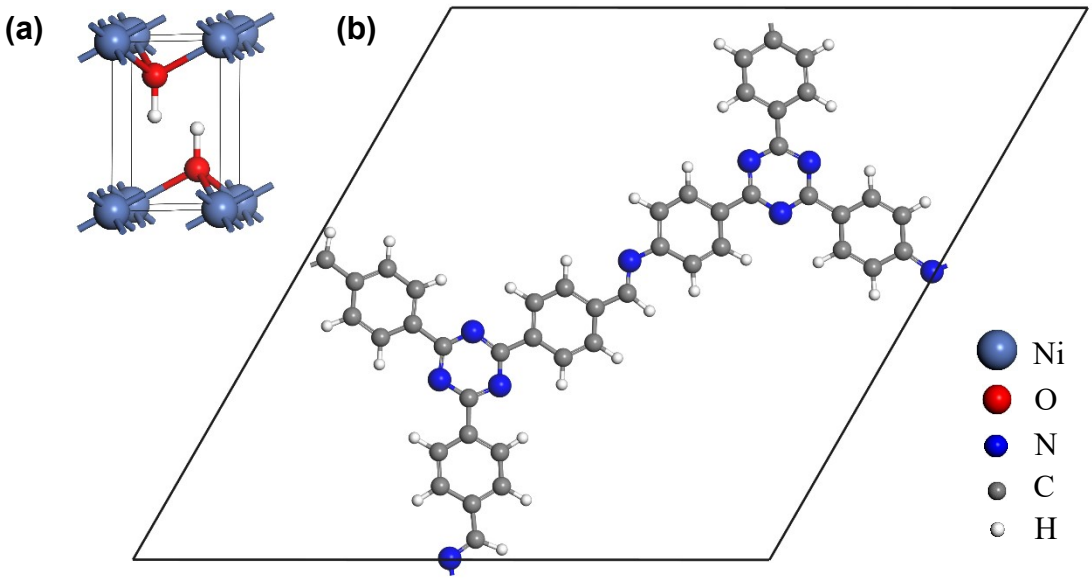

Figure S20. Schematic of the $Ni(OH)_2$ crystal structure (a) and COF crystalline porous material (b). The atoms are represented by spheres: Ni (purple, large), O (red, intermediate between large and medium), N (blue, medium), C (gray, intermediate between medium and small), and H (white, small).

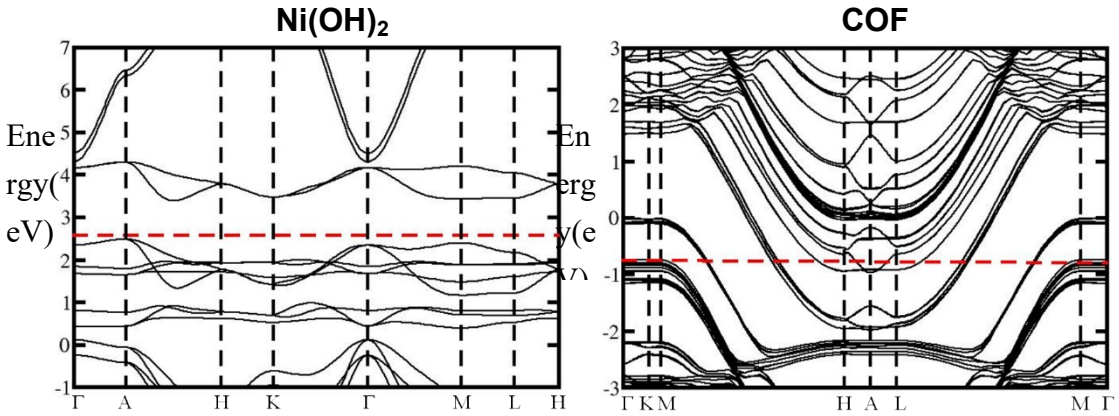

Figure S21. The left and right panels illustrate the electronic band structures of the $Ni(OH)_2$ model, with a band gap of 0.907 eV, and the COF model, with a band gap of 1.487 eV. The red dashed lines represent the Fermi levels, while the black dashed lines indicate the reciprocal space paths in the first Brillouin zone.

3. Supplementary Table

Table S1 Comparison of UOR performances of various electrocatalysts reported in the literature.

Catalysts	Electrolyte	Current density and/or mass activity at 1.5 (V vs. RHE)	Stability test
$Ni(OH)_2$/COF/CNT this work	**1 M KOH + 0.33 M urea**	**153 mA cm^{-2} 153 A g^{-1} 363 A $g_{Ni(OH)2}^{-1}$**	**24 h @ 20 mA cm^{-2}**
$Ni(OH)_2$-based electrocatalysts			
Co-doped α-$Ni(OH)_2$[17]	1 M KOH + 0.33 M urea	~45 mA cm^{-2} ~707 A g^{-1}	24 h @ 1.41 V
Co–$Ni(OH)_2$[18]	1 M KOH + 0.33 M urea	>350 mA cm^{-2} >18 A g^{-1}	100 h @10 mA cm^{-2}
Mn-doped NiCo LDH/CNT[19]	1 M KOH + 0.50 M urea	~175 mA cm^{-2} ~35 A g^{-1}	24 h @ 1.35 V
Heterostructured electrocatalysts			
NiS_2/SnS_2[20]	1 M KOH + 0.33 M urea	~75 mA cm^{-2} ~180 A g^{-1}	12 h @1.37 V
Ni_3S_2–Ni_3P[21]	1 M KOH + 0.5 M urea	>150 mA cm^{-2}	20 h @ 1.5 V
NiF_3/Ni_2P [22]	1 M KOH +	~70 mA cm^{-2}	10h @ 10 mA cm^{-2}

	0.33 M urea	~11 A g^{-1}	
Heterojunction electrocatalysts			
CoS_2-MoS_2[23]	1 M KOH + 0.50 M urea	> 350 mA cm^{-2}	30 h @ 10 mA cm^{-2}
$CoMn/CoMn_2O_4$[24]	1 M KOH + 0.50 M urea	> 300 mA cm^{-2} >250 A g^{-1}	16.7 h @ 20 mA cm^{-2}
$NiSe_2/FeSe_2$[25]	1 M KOH + 0.33 M urea	> 140 mA cm^{-2} > 467 A g^{-1}	15 h @ 10 mA cm^{-2}
MoS_2/Ni_3S_2[26]	1 M KOH + 0.50 M urea	> 200 mA cm^{-2}	24 h @ 10 mA cm^{-2}
NiS/MoS_2[27]	1 M KOH + 0.50 M urea	> 300 mA cm^{-2}	25 h @ 1.5 V
CoS_x-MoO_x@NF[28]	1 M KOH + 0.33 M urea	~43 mA cm^{-2}	1000 CV cycles between ~1.1 and ~1.5 V
$Se/NiSe_2$[29]	1 M KOH + 0.33 M urea	> 400 mA cm^{-2} > 267 A g^{-1}	20 h @ 1.45 V with sea water

Table S2 Calculated equilibrium lattice constants of the $Ni(OH)_2$ crystal structure and COF crystalline porous material. $Ni(OH)_2$ results are much closer to the other theoretical values.[30, 31]

	Lattice constant (Å)			Angle (°)		
	a	*b*	*c*	*α*	*β*	*γ*
$Ni(OH)_2$	3.20, 3.12[30]	3.20, 3.12[30]	4.40, 4.66[30]	90.00	90.00	120.00
COF	25.24, 25.71[31]	26.05, 25.71[31]	2.72	90.00	90.00	120.00

4. References

1. A. F. M. El-Mahdy, C. H. Kuo, A. Alshehri, C. Young, Y. Yamauchi, J. Kim and S. W. Kuo, *J. Mater. Chem. A*, 2018, **6**, 19532.
2. J. P. Jyothibasu, D. W. Kuo and R. H. Lee, *Cellulose*, 2019, **26**, 4495.
3. H. C. Yang, Y. Y. Chen, S. Y. Suen and R. H. Lee, *Polymer*, 2023, **273**, 125853.
4. J. P. Perdew and W. Yue, *Phys Rev B Condens Matter*, 1986, **33**, 8800.
5. G. Kresse and J. Furthmüller, *Comput. Mater. Sci.*, 1996, **6**, 15.
6. G. Kresse and J. Hafner, *J. Phys.: Condens. Matter*, 1994, **6**, 8245.
7. G. Kresse and J. Furthmüller, *Phys. Rev. B*, 1996, **54**, 11169.
8. M. Aghazadeh, M. Ghaemi, B. Sabour and S. Dalvand, *J. Solid State Electrochem.*, 2014, **18**, 1569.
9. S. Anantharaj, P. E. Karthik and S. Noda, *Angew. Chem. Int. Ed.*, 2021, **60**, 23051.
10. R. K. Singh and A. Schechter, *Electrochim. Acta*, 2018, **278**, 405.
11. Q. Dong, C. Zhu, M. Chen, C. Jiang, J. Guo, Y. Feng, Z. Dai, S. K. Yadavalli, M. Hu, X. Cao, Y. Li, Y. Huang, Z. Liu, Y. Shi, L. Wang, N. P. Padture and Y. Zhou, *Nat. Commun.*, 2021, **12**, 973.
12. J. Ran, J. Yu and M. Jaroniec, *Green Chem.*, 2011, **13**.
13. J. Yu, S. Wang, B. Cheng, Z. Lin and F. Huang, *Catal. Sci. Technol.*, 2013, **3**, 1782.
14. J. Bi, W. Fang, L. Li, J. Wang, S. Liang, Y. He, M. Liu and L. Wu, *Macromol. Rapid Commun.*, 2015, **36**, 1799.
15. I. Vamvasakis, I. T. Papadas, T. Tzanoudakis, C. Drivas, S. A. Choulis, S. Kennou and G. S. Armatas, *ACS Catal.*, 2018, **8**, 8726.
16. N. Singh, D. Yadav, S. V. Mulay, J. Y. Kim, N. J. Park and J. O. Baeg, *ACS Appl. Mater. Interfaces*, 2021, **13**, 14122.
17. Y. Liu, Z. Yang, Y. Zou, S. Wang and J. He, *Energy Environ. Mater.* , 2023, **0**,

e12576.
18. Y. Wang, Y. Lu, Y. Shi, J. Wang, Y. Zheng, J. Pan, C. Li and J. Cao, *Appl. Surf. Sci.*, 2023, **640**, 158391.
19. K. Wu, C. Cao, K. Li, C. Lyu, J. Cheng, H. Li, P. Hu, J. Wu, W.-M. Lau, X. Zhu, P. Qian and J. Zheng, *Chem. Eng. J.*, 2023, **452**, 139527.
20. Z. Ji, J. Liu, Y. Deng, S. Zhang, Z. Zhang, P. Du, Y. Zhao and X. Lu, *J. Mater. Chem. A*, 2020, **8**, 14680.
21. J. Liu, Y. Wang, Y. Liao, C. Wu, Y. Yan, H. Xie and Y. Chen, *ACS Appl. Mater. Interfaces*, 2021, **13**, 26948.
22. K. Wang, W. Huang, Q. Cao, Y. Zhao, X. Sun, R. Ding, W. Lin, E. Liu and P. Gao, *Chem. Eng. J.*, 2022, **427**, 130865.
23. C. Li, Y. Liu, Z. Zhuo, H. Ju, D. Li, Y. Guo, X. Wu, H. Li and T. Zhai, *Adv. Energy Mater.*, 2018, **8**, 1801775.
24. C. Wang, H. Lu, Z. Mao, C. Yan, G. Shen and X. Wang, *Adv. Funct. Mater.*, 2020, **30**, 2000556.
25. S. Ni, H. Qu, Z. Xu, X. Zhu, H. Xing, L. Wang, J. Yu, H. Liu, C. Chen and L. Yang, *Appl. Catal. B-Environ.*, 2021, **299**, 120638.
26. Y. Ren, C. Wang, W. Duan, L. Zhou, X. Pang, D. Wang, Y. Zhen, C. Yang and Z. Gao, *J. Colloid Interface Sci.*, 2022, **628**, 446.
27. C. Gu, G. Zhou, J. Yang, H. Pang, M. Zhang, Q. Zhao, X. Gu, S. Tian, J. Zhang, L. Xu and Y. Tang, *Chem. Eng. J.*, 2022, **443**, 136321.
28. Q. Zhang, C. Cui, Z. Wang, F. Deng, S. Qiu, Y. Zhu and B. Jing, *Sci. Total Environ.*, 2023, **858**, 160170.
29. S. Khatun and P. Roy, *J. Colloid Interface Sci.*, 2023, **630**, 844.
30. A. J. Tkalych, K. Yu and E. A. Carter, *The Journal of Physical Chemistry C*, 2015, **119**, 24315.
31. Y. Wan, L. Wang, H. Xu, X. Wu and J. Yang, *J. Am. Chem. Soc.*, 2020, **142**, 4508.